
Full-dose PET Synthesis from Low-dose PET Using High-efficiency Diffusion Denoising Probabilistic Model

Shaoyan Pan^{1,2}, Elham Abouei¹, Junbo Peng¹, Joshua Qian¹, Jacob F Wynne¹, Tonghe Wang³,
Chih-Wei Chang¹, Justin Roper¹, Jonathon A Nye⁴, Hui Mao⁵ and Xiaofeng Yang^{1,2*}

¹Department of Radiation Oncology and Winship Cancer Institute, Emory University, Atlanta, GA 30322,
USA

²Department of Biomedical Informatics, Emory University, Atlanta, GA 30322, USA

³Department of Medical Physics, Memorial Sloan Kettering Cancer Center, New York, NY 10065, USA

⁴Radiology and Radiological Science, Medical University of South Carolina, Charleston, SC 29425, USA

⁵Department of Radiology and Imaging Science, and Winship Cancer Institute, Emory University,
Atlanta, GA 30322, USA

*Email: xiaofeng.yang@emory.edu

Running title: Low Dose PET Imaging

Manuscript Type: Original Research

Key words: Consistency model, Denoising diffusion probabilistic model, Swin transformer, image synthesis, PET synthesis

Abstract

Purpose: To reduce the risks associated with ionizing radiation, a reduction of the radiation exposure in PET imaging is needed. However, this leads to a detrimental effect on image contrast and quantification. To address this challenge, low dose PET images synthesized from low-dose data offers a potential solution to reduce radiation exposure while maintaining high-quality PET images suitable for the clinical setting.

Methods: We introduce an efficient diffusion-model-based approach for estimating full-dose PET images from low-dose PET images: the PET Consistency Model (PET-CM) yielding synthetic quality comparable to state-of-the-art diffusion-based synthesis models, but with greater efficiency. This method involves a two-step process: a forward process that adds Gaussian noise to a full dose PET image at multiple timesteps, and a reverse diffusion process that employs a PET Shifted-window Vision Transformer (PET-VIT) network to learn the denoising procedure conditioned on the corresponding low-dose PETs. Thus, low-dose PETs can be translated to full-dose PETs. In PET-CM, the reverse process learns a consistency function that produces the same output for all possible inputs of a noisy image at each timestep, enabling direct denoising of Gaussian noise to a clean full-dose PET. The PET-VIT comprises a U-shaped encoder-decoder architecture consisting of convolutional layers for capturing local features and Swin attention layers for capturing global features, ensuring accurate performance of the reverse processes. We evaluated the PET-CM in generating full-dose images from low-dose images using only one eighth and one quarter of the standard PET dose. The quality of the synthesized full-dose images was assessed by comparing them with ground truth full dose PET images using normalized mean absolute error (NMAE), peak signal-to-noise ratio (PSNR), multi-scale structural similarity index (MS-SSIM) and normalized cross-correlation (NCC).

Results: In experiments comparing 1/8 dose to full-dose images, PET-CM demonstrated impressive performance with NMAE of $1.233\pm 0.131\%$, PSNR of $33.915\pm 0.933\text{dB}$, SSIM of 0.964 ± 0.009 , and NCC of 0.968 ± 0.011 , with an average generation time of 62 seconds per patient. This is a significant improvement compared to the state-of-the-art diffusion-based model with PET-CM reaching this result 12x faster. Similarly, in the 1/4 dose to full-dose image experiments, PET-CM delivered competitive outcomes, achieving an NMAE $1.058\pm 0.092\%$, PSNR of $35.548\pm 0.805\text{dB}$, SSIM of 0.978 ± 0.005 , and NCC 0.981 ± 0.007 using the same generation process.

Conclusions: We propose PET-CM, an efficient diffusion-model-based method, for estimating full-dose PET images from low-dose images. PET-CM provides comparable quality to the state-of-the-art diffusion model with higher efficiency. This method offers promising improvements in low-dose PET image quality, making them suitable for potential clinical applications.

I. Introduction

Positron emission tomography (PET) imaging has broad clinical applications, including disease diagnosis in oncology (Unterrainer *et al.*, 2020), cardiology (Slomka, 2022), and neurology (Verger *et al.*, 2022); determining disease stage, lesion malignancy, and response to treatment (Kaplan and Zhu, 2018); and co-registration with computed tomography (CT) or magnetic resonance imaging (MRI) scans to visualize both anatomic and metabolic localization (Chaudhari *et al.*, 2021). One of the most important tradeoffs in PET imaging is between image quality and radiation exposure. Improving image quality is desirable for all clinical applications, while minimizing radiation exposure is needed to reduce risk to patients. The radiation exposure from a PET-CT scan can be substantial: 25 millisieverts (mSv) for a 70 kg person, compared to just 0.1 mSv for a chest x-ray (Brix *et al.*, 2005; Huda *et al.*, 1989).

In photon-count limited modalities like PET, noise affects image quality and is inherent in the data due to low sensitivity of PET scanners. To enhance signal-to-noise ratio (SNR), more radiotracer is administered, resulting in greater radiation exposure. Minimizing the administered radiotracer while maintaining image quality can be achieved through hardware and software advancements. Equipment manufacturers have focused primarily on a hardware approach to push PET scanning to detect a larger fraction of annihilation photons and improve sensitivity (Cherry *et al.*, 2017). Various signal-processing techniques have also been developed to minimize the contribution of noise, improving image quality. These techniques include standard smoothing routinely applied after image reconstruction, image denoising techniques, and approaches that use information obtained from another imaging modality, such as CT or MRI. Soon, the prospect of combining both hardware and software approaches including ultra-high sensitivity PET scanners, simultaneously acquired CT/MRI data, and machine learning algorithms to improve the PET image quality could become a reality. These advances would allow dramatic reductions of administered radiotracer or scan time required for obtaining excellent quality PET images and transform PET into a near-nonionizing imaging modality (Catana, 2019).

Machine learning approaches in medical imaging allow us to expand upon technological and hardware advances. These include multilevel canonical correlation analysis (An *et al.*, 2016), mapping-based sparsified representation (Wang *et al.*, 2016), semisupervised triple dictionary learning (Wang *et al.*, 2018), as well as deep learning approaches (Chaudhari *et al.*, 2021; Kaplan and Zhu, 2018; Wang *et al.*, 2020; Dong *et al.*, 2020; Zhang *et al.*, 2021) using deep auto-context convolutional neural networks (CNN) (Xiang *et al.*, 2017). The performances of these approaches depend on handcrafted features extracted based on prior domain knowledge, as well as small-patch-based methods that tend to generate over-smoothed images resulting in a loss of texture information. The application of these data-driven methods can be complicated and cumbersome on whole-body images. Other methods include three-dimensional conditional generative

adversarial networks (CGAN) (Wang *et al.*, 2018), cycle-consistent GAN (Lei *et al.*, 2019), denoising diffusion probabilistic models (DDPM) (Gong *et al.*, 2022), and improved DDPM (IDDPM) (Pan *et al.*, 2023a; Pan *et al.*, 2023b; Pan *et al.*, 2023c). Diffusion and score matching models present an alternative generative approach, drawing inspiration from the study of non-equilibrium thermodynamics in physics. DDPM methods are a category of distribution learning-based models which employ a Markov chain of diffusion steps to systematically introduce random noise into data and subsequently learn to reverse the diffusion process, generating desired data samples from the noise (Ho *et al.*, 2020; Song *et al.*, 2020). They are advantageous over GANs by leading to improved training stability and the production of more authentic and higher-quality synthetic images (Pan *et al.*, 2023c), but require much more time to generate images. Accordingly, Song *et al.* proposed a Consistency Model (CM) which can generate images with quality comparable to DDPMs, but with much higher efficiency (Song *et al.*, 2023). These machine learning-based frameworks may be used to predict standard- or full-dose PET images from much lower dose PET images. In this study, we present an efficient diffusion-based method for estimating whole-body full-dose PET images. The PET Consistency Model (PET-CM) offers comparable performance to the state-of-the-art diffusion model, but with enhanced efficiency. To evaluate effectiveness, we compare these methods with three previously proposed approaches and conduct a quantitative analysis of synthetic full-dose images generated by PET-CM. We comparing them to PET-CGAN, PET-cycleGAN, PET-DDPM, and PET-IDDPM using eighth- and quarter- dose PET images. The results demonstrate that the proposed PET-CM outperforms the other methods as measured by the selected quantitative indices.

II. Method

The proposed PET-CM uses a denoising neural network to convert a two-dimensional Gaussian noisy sample $X_T \sim \mathcal{N}(0,1)$ into a corresponding full-dose PET conditioned on a given low-dose PET. The PET-CM is based on a crucial assumption: by iteratively adding a small amount of noise ϵ to a real full-dose scan X_0 over a certain number of timesteps (T), we can transform X_0 into a purely Gaussian noise sample X_T . This assumption holds when the number of timesteps (t) is sufficiently large. As a result, a full-dose PET can be obtained by removing added noise from a noisy sample. This principle applies not only to specific noise samples but can be generalized to any noise sample. In addition, a low-dose PET scan is incorporated to guide the denoising process and generate paired full-dose PET for the same patient. This integration of the low-dose PET helps to guide and control the diffusion process, resulting in a full-dose PET that is specifically associated with the corresponding patient.

The proposed PET-CM comprises two main steps: a forward process, where Gaussian noise is incrementally added to the full-dose PETs, and a reverse process, which is learned by the proposed denoiser network called PET Vision Transformer network (PET-VIT). The purpose of the reverse process is to

efficiently eliminate the Gaussian noise present in the noisy full-dose PET images. While most diffusion models estimate the reverse distribution for X_t and X_{t-1} at each timestep t , enabling the recursive generation of X_0 through multiple timesteps; PET-CM estimates a function that directly connects X_T to X_0 . This direct connection allows for the generation of X_0 in just a few steps, bypassing the need for extensive recursion.

Figure 1.a) illustrates the design of PET-VIT, which is based on Pan *et al.*'s (Pan *et al.*, 2023c) denoiser architecture. The architecture comprises a two-dimensional encoder and decoder. The encoder includes down-sampling residual convolutional blocks and Shifted-window self-attention (Swin-SA) blocks (Liu *et al.*, 2021), which enable the learning of semantic features at various resolution levels. Conversely, the decoder exhibits a symmetrical structure to the encoder and is responsible for reconstructing the final estimations using the learned semantic features. Below, we provide a detailed description of the network architecture and the mathematical formulation for PET-CM.

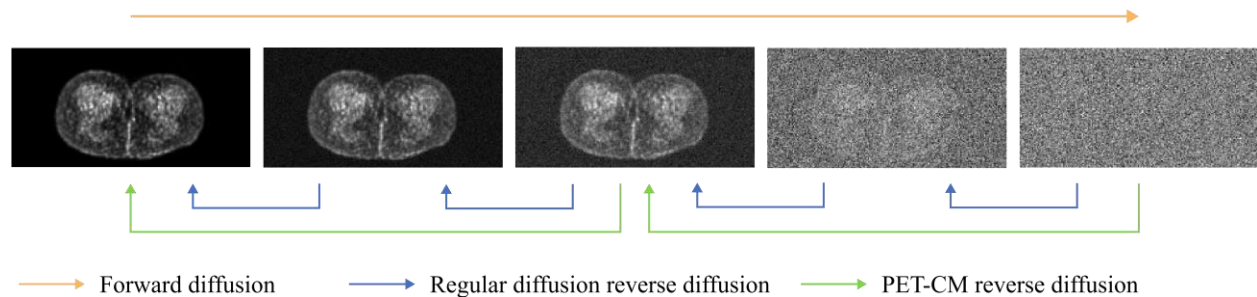


Figure 1: The denoising diffusion process of PET-CM employs a forward diffusion process to introduce Gaussian noise to full-dose PETs using multiple timesteps, gradually transforming them into pure Gaussian noise. Subsequently, the regular diffusion models utilize a reverse diffusion process to iteratively denoise the images from each timestep $t - 1$ to t , effectively reducing noise. In contrast, PET-CM generates clean images with larger intervals between timesteps, providing efficient denoising without requiring a large number of iterations.

II.A Network architecture

The complete architecture is depicted in Fig 1. b). Starting with the encoder, the input undergoes a convolutional layer with a 3×3 kernel size and stride of 1 to capture early features. These features are then down-sampled by a factor of 2 in each block. In the encoder architecture, we propose one initial down-sampled convolutional block to learn local characteristics from inputs with higher resolutions. Subsequently, we incorporate three sequential down-sampled Swin-transformer blocks to capture global information from lower-resolution features. Following this, two middle Swin-transformer blocks (without down-sampling or up-sampling) are connected to further extract global characteristics. The decoder consists of three up-sampled Swin-transformer blocks and one final up-sampled convolutional blocks to obtain the

features with the original resolution. Eventually, the resulting features are fed into one convolutional layer to estimate the consistency function. Additionally, we utilize the residual connection (He *et al.*, 2016) (as shown in Fig. 1.c) in each convolutional and Swin-SA block to enhance network stability. Furthermore, we employ shortcut connections across the blocks (as shown in Fig. 1.b), connecting each encoder block to a decoder block at the same resolution level. This facilitates the transmission of high-resolution information from the encoder to the decoder, enhancing estimation accuracy.

On the other hand, the timesteps t are encoded using sinusoidal embedding (SE) (Dhariwal and Nichol, 2021), where the maximum period of SE is set as 10^6 , and the feature dimension is set as 128. These timestep embeddings are input into all blocks so the network denoises the input PET according to the corresponding timestep. More specifically, the embedded timesteps $F \in \mathbb{R}^{1 \times d}$ are first passed into a timestep expanding linear layer to obtain a scale feature map $sc \in \mathbb{R}^{1 \times d_s}$ and shift map $sh \in \mathbb{R}^{1 \times d_s}$, where d is the sinusoidal embedded timestep’s dimension and d_s is the semantic feature map dimension. The sc and sh maps are then summed to the output of the first layer of each block C (e.g., the first up/down-sampled layer of the up/down-sampled convolutional/Swin-SA blocks) via scale shift normalization:

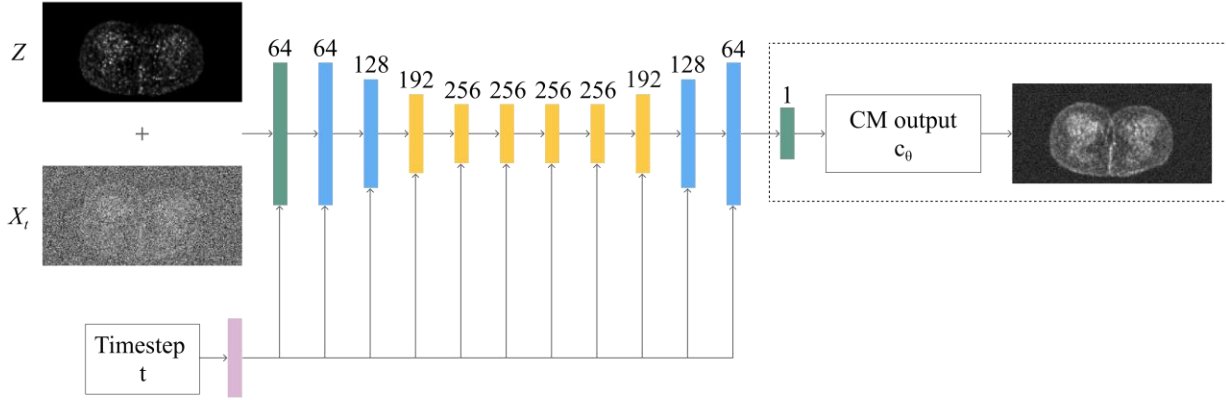
$$output = C * (1 + sc) + sh \quad [1]$$

The output is subsequently fed into subsequent convolutional/Swin-SA layers, enabling each convolutional section to learn semantic information conditioned on the timestep t .

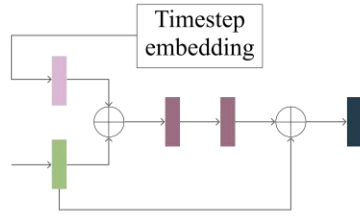
II.B Diffusion model

Following Pan et al (Pan *et al.*, 2023c) and Saharia et al (Saharia *et al.*, 2022), a standard conditional diffusion model consists of three processes: First, a forward diffusion process gradually applies small amounts of Gaussian noise N to an initial full dose PET image X_0 over a series of T timesteps. This transforms the PET scan into pure multi-dimensional Gaussian noise X_T . Next, the proposed PET-CM denoiser (the proposed network) is trained to learn a reverse diffusion process, taking into account the low dose PET Z as a conditioning factor. This reverse process effectively removes the small amounts of noise added at each timestep, ultimately denoising X_T and restoring it to the original PET scan X_0 . Finally, by employing an optimal PET-CM denoiser, we can run a sampling process to recursively translate a pure Gaussian noise to a full dose PET image corresponding to the input low dose PET.

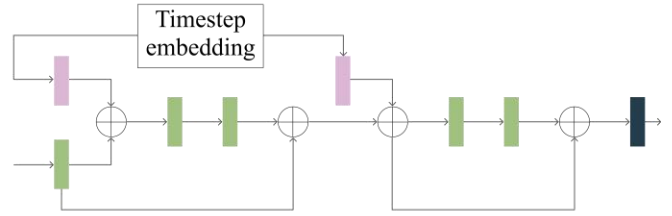
a) PET-IDDPM/CM architecture



b) Swin-transformer layer



c) Convolutional layer



- 1x1 convolutional layer ■ Convolutional block ■ Swin transformer block ■ Down/Up sampling layer
- 3x3 Convolutional layer ■ Linear layer ■ Swin layer

Figure 2: a) Network architectures of PET-VIT used in PET-CM: A symmetrical encoder-decoder architecture is employed to learn the reverse process, in which PET-CM learns a consistency function for generating full dose images. b) Swin-transformer block: The purple Swin layer consists of a window self-attention and a shifted window self-attention module. c) Convolutional block: Three convolutional residual structures are utilized to learn local features.

II.B.1 Forward diffusion process

During the forward diffusion process, we aim to generate noisy images $[X_1, X_2, \dots, X_T]$ so we can have data to train the PET-CM denoiser. The generation of the noisy image at timestep t is determined exclusively by the noisy image at timestep $t - 1$. Specifically, the process of generating the noisy image can be described as a Markov process, where the transition probability from image X_{t-1} to image X_t follows a Gaussian distribution denoted as \mathcal{N} with a pre-determined variance β_t .

$$q(X_t|X_{t-1}) = \mathcal{N}(X_t; \sqrt{1 - \beta_t}X_{t-1}, \beta_t I) \quad [2]$$

Using reparameterization (Ho *et al.*, 2020), we can efficiently generate noisy full-dose PET at any arbitrary timestep t with noise sampled $\epsilon_t \sim \mathcal{N}(0, I)$ from a normal distribution:

$$X_t = \sqrt{\alpha_t}X_0 + \sqrt{1 - \alpha_t}\epsilon_t \quad [3]$$

where $\alpha_t = \prod_{i=0}^t (1 - \beta_i)$. The selection of the maximum timestep T is 1000 and β_t is $5e^{-6}t$ for all diffusion model experiments.

II.B.2 Reverse diffusion process

In the reverse diffusion process, we train the network θ to estimate the inverse Gaussian distribution $q(X_{t-1}|X_t)$ (Dhariwal and Nichol, 2021) so we can recursively move in a reverse direction from X_T to X_0 . In contrast to unconditional diffusion model synthesis (Pan *et al.*, 2023c; Nichol and Dhariwal, 2021), we introduce a novel approach by incorporating low-dose PET scans. By including the low-dose PET as a conditioning factor, the denoiser is guided along a specific denoising path. This conditioning enables the generation of a full-dose PET image that corresponds to the given low-dose PET input. Practically, all functions with conditions “ $f: (X_t, t|Z) \rightarrow \text{output}$ ” in the following sections refer to a specific input configuration. In this configuration, one of the inputs for the function is created by concatenating the data X_t and Z , while the other input corresponds to the timestep t .

II.C Consistency model (Efficient diffusion model)

II.C.1 Continuous forward diffusion process

Assuming a large timestep T , we can generalize the forward and reverse diffusion process into continuous-time processes to be solved in the form of a Stochastic Differential Equation (SDE). We follow Song *et al.*’s work (Song *et al.*, 2020) to develop the forward SDE process:

$$dX_t = f(X_t, t)dt + g(t)dw_t \quad [4]$$

where dw_t is a normal noise. Accordingly, we have a Probability Flow ordinary differential equation (PF-ODE) reverse process

$$dX_t = \left[f(X_t, t) - \frac{1}{2}g^2(t)\nabla \log p_t(X_t) \right] dt \quad [5]$$

By setting $f(X_t, t) = 0$ and $g(t) = \sqrt{2t}$, we arrive at:

$$\frac{dX_t}{dt} = -tS_\theta(X_t, t) \quad [6]$$

where $S_\theta(X_t, t)$ is the estimation of the score function $\nabla \log p_t(X_t)$ and the PF-ODE can be solved by any numerical ODE solver, such as Heun’s method (Song *et al.*, 2023) (details shown in Appendix B).

II.C.2 Consistency Model

Obtaining the clean image X_0 using ODE solvers requires iterative evaluations of the score model $S_\theta(X_t, t)$, which is a computationally costly process. To accelerate sampling, the self-consistency property is introduced to arbitrary pairs of (X_t, t) , under the guidance of Z , in the same PF-ODE trajectory, which is formulated as:

$$c_\theta(X_t, t, Z) = c_\theta(X_\epsilon, \epsilon, Z) = X_\epsilon \approx X_0, t \in [\epsilon, T] \quad [7]$$

where c_θ is the consistency function learned by the network θ , mapping all the points in the trajectory to the destination of the trajectory X_0 , and the consistency function is estimated by a neural network model θ . ϵ is a scalar sufficiently close to 0. We can thus translate a pure Gaussian noise X_T into a full dose PET X_0 conditioning on a low-dose PET Z and, in an extreme case, the full-dose PET can be generated by one step as $X_0 \approx c(X_T, T, Z)$.

II.C.2.A Consistency forward process

First, we need to build a set of timesteps $t = [t_1, t_2, \dots, t_j]$ suitable for the consistency model:

$$t_j = \left(\frac{1}{\epsilon^\rho} + \frac{j-1}{J-1} \left(T^{\frac{1}{\rho}} - \frac{1}{\epsilon^\rho} \right) \right)^\rho \quad [8]$$

where we empirically set the minimum noise scale $\epsilon = 0.002$, the maximum noise scale $T = 80$, the number of timesteps $J = 150$, and noise power $\rho = 7$. Then, we can generate the noisy full dose PET X_{t_j} at timestep t_j :

$$X_{t_j} = X_0 + t_j \epsilon_{t_j} \quad [9]$$

where $\epsilon_{t_j} \sim \mathcal{N}(0, I)$ is a random normal noise.

II.C.2.B Consistency Training

A straightforward way to train the consistency model c_θ is to perform distillation of the pre-trained score function S_θ , which is called the consistency distillation (CD) method. However, the CD strategy requires pre-trained model training on an extremely large-scale dataset, which is impractical in medical image synthesis. Alternatively, we can directly train the consistency model without knowledge of the score model S_θ in what is called the consistency training (CT) method. In the CT strategy, we avoid the pre-trained score model by leveraging the unbiased estimator (Song *et al.*, 2023)

$$\nabla \log p_t(X_t, Z) = -E \left[\frac{X_t - X_0}{t^2} \mid X_t, Z \right] \quad [10]$$

and the loss function can be formulated as:

$$L = MAE \left(c_\theta(X_{t_j}, t_j, Z), c_\theta(X_{t_{j-1}}, t_{j-1}, Z) \right) \quad [11]$$

where t_j and t_{j-1} are adjacent time steps for the same PF-ODE trajectory. The loss function is designed to minimize the output of two adjacent data points $(X_{t_{j-1}}, t_{j-1})$ and (X_{t_j}, t_j) . When the subscript j runs through all possible steps, the consistency property of c_θ is enforced on all the data points in the same trajectory.

Following Song (Song *et al.*, 2023), we employed the exponential moving average (EMA) technique to

boost the convergence of the optimization problem. Specifically, the optimization process requires two identical networks: θ and θ' . The loss function is minimized by stochastic gradient descent on the model parameter set θ , while updating θ' with the EMA of θ . The modified loss function can be expressed as:

$$L = MAE \left(c_{\theta}(X_{t_j}, t_j, Z), c_{\theta'}(X_{t_{j-1}}, t_{j-1}, Z) \right) \quad [12]$$

II.C.3 Consistency Sampling

With a well-trained consistency denoiser θ , we can generate a full-dose PET image at timestep t_j , at any arbitrary timestep t_j :

$$X_{t_j} = c_{\theta}(X_{t_j}, t_j, Z) + \sqrt{t_j^2 - \varepsilon^2} \epsilon_{t_j} \quad [13]$$

In our consistency model experiments we adopt two-step generation using the set of timesteps $t = [1, 75, 150]$ for inference and X_{t_1} is the final synthetic full dose PET. To account for the randomness introduced during the generation process, each sPET image is generated three times and the final output is obtained by averaging the results. This approach follows a Monte Carlo-based (MC-based) generation method, which helps to mitigate the impact of random noise and improve the overall stability and reliability of the generated synthetic PETs (sPETs). (Lyu and Wang, 2022).

III. Data acquisition

III.A Institutional whole-body PET dataset

The dataset consists of 35 patients (11,200 slices) from whole-body ^{18}F -FDG PET/CT. The first 22 patients (7,040 slices) were utilized for model training, and the remaining 13 patients (4,160 slices) were withheld for testing. Images were acquired using a GE Discovery 690 PET/CT scanner. 370 MBq and 444 MBq ^{18}F -FDG radiotracer was administered for patients with BMI less than or greater than 30, respectively, followed by 60-minute uptake period. A 3D ordered-subset expectation maximization (OSEM) algorithm of 3 iterations and 24 subsets was used for image reconstruction, and a CT-based attenuation correction was applied. To create low-dose PET data, two additional sets of PET data were histogram-reduced to one eighth and one quarter of the original bed duration for all bed positions.

All training and test low-dose PETs were centered and cropped to a size of 96 x 192 x 320 with a pixel size of 3.65 x 3.65 x 3.27 mm³. PET intensities were then jointly normalized to [-1, 1]. Networks were trained and tested on 2D axial slices. These slices were subsequently combined to reconstruct a complete whole-body scan for evaluation. To ensure consistency, a patch size of 64 x 64 was selected and we employed the same patch-based input approach and sliding window prediction technique for both the low-dose dataset during training and inference. During training, we utilized an AdamW optimizer with an initial learning rate of 2×10^{-5} and a weight decay of 1×10^{-4} across 500 epochs to train PET-CM. In the PET-CM experiments, the model was trained with 150 timesteps and generated full dose PETs with 2 steps ($t =$

[1,75,150]).

IV. Implementation and performance evaluation

IV.A Implementation details

The PET-CM frameworks and competing networks were executed on a workstation running Microsoft Windows 11 equipped with a single NVIDIA RTX 6000 GPU with 48 gigabytes of memory. The experiments were conducted using the PyTorch framework in Python version 3.8.11.

IV.B Quantitative evaluation

The quality of the synthetic PET generated by the proposed PET-CM were evaluated using the normalized mean absolute error (MAE in percentage of the activity concentration value per volume), peak signal-to-noise ratio (PSNR in decibel), multi-scale structure similarity index (MS-SSIM, with an evaluation scale of 3) and maximum normalized cross correlation (NCC) indices. NMAE is a negatively-oriented score: a smaller value indicates a smaller absolute difference between the ground truth PET and the sPET, implying better sPET quality. PSNR, SSIM and NCC are positively-oriented: higher PSNR indicates a higher peak signal similarity, higher SSIM indicates greater overall visual similarity, and higher NCC indicates better image correlation between the sPET and real PET. All metrics were background excluded and calculated at the patient level. To establish a benchmark, we compared the proposed networks' performance against state-of-the-art low-dose to full-dose PET conversion methods, including PET-CGAN (Lei *et al.*, 2019), PET-cycleGAN (Lei *et al.*, 2019), PET-DDPM (Ho *et al.*, 2020), and PET-IDDPM (Nichol and Dhariwal, 2021). We configured the GAN-based networks as detailed in their corresponding references. For PET-DDPM and PET-IDDPM, we adopted the same network architecture from PET-CM for equipoise. We applied identical training hyperparameters for all networks, including patch size, optimizer, learning rate, training and generation timesteps (applicable only for diffusion-based methods), and data preprocessing. We conducted pair-wise comparisons using one-sampled Student's paired t-test with $\alpha = 0.05$.

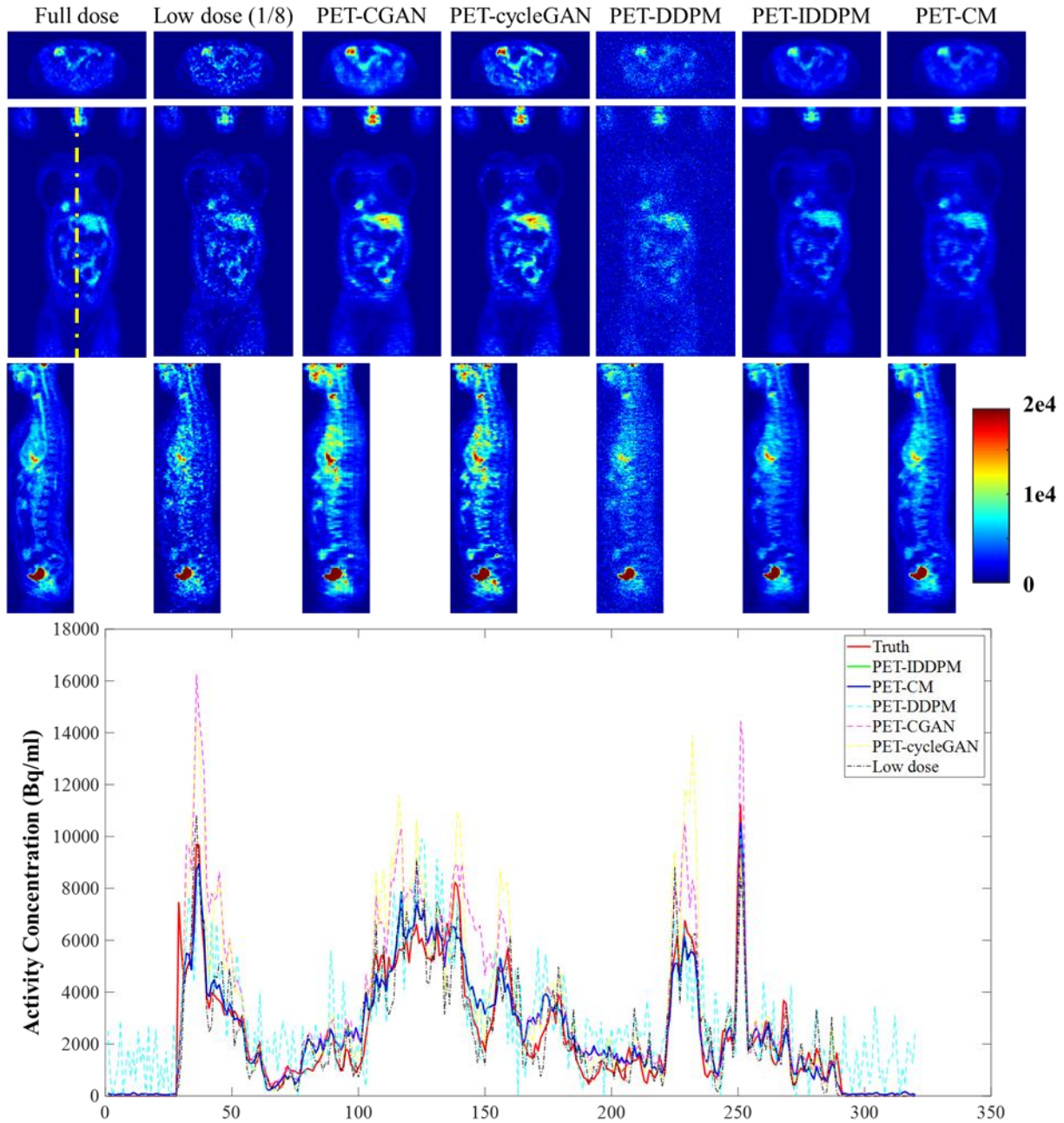


Figure 3: Visualization of the imaging results and single line profiles for the synthetic images obtained from eighth dose PETs. The figure displays the full dose image (1st column), the corresponding low dose image (2nd column), and the synthesized images generated by different methods: PET-DDPM (3rd column), PET-CGAN (4th column), PET-cycleGAN (5th column), PET-IDDPM (6th column), and PET-CM (7th column). The single line profiles are shown below the visualizations, illustrating the variations in intensity along the line for both the real and synthetic images. Red represents ground truth full-dose PET.

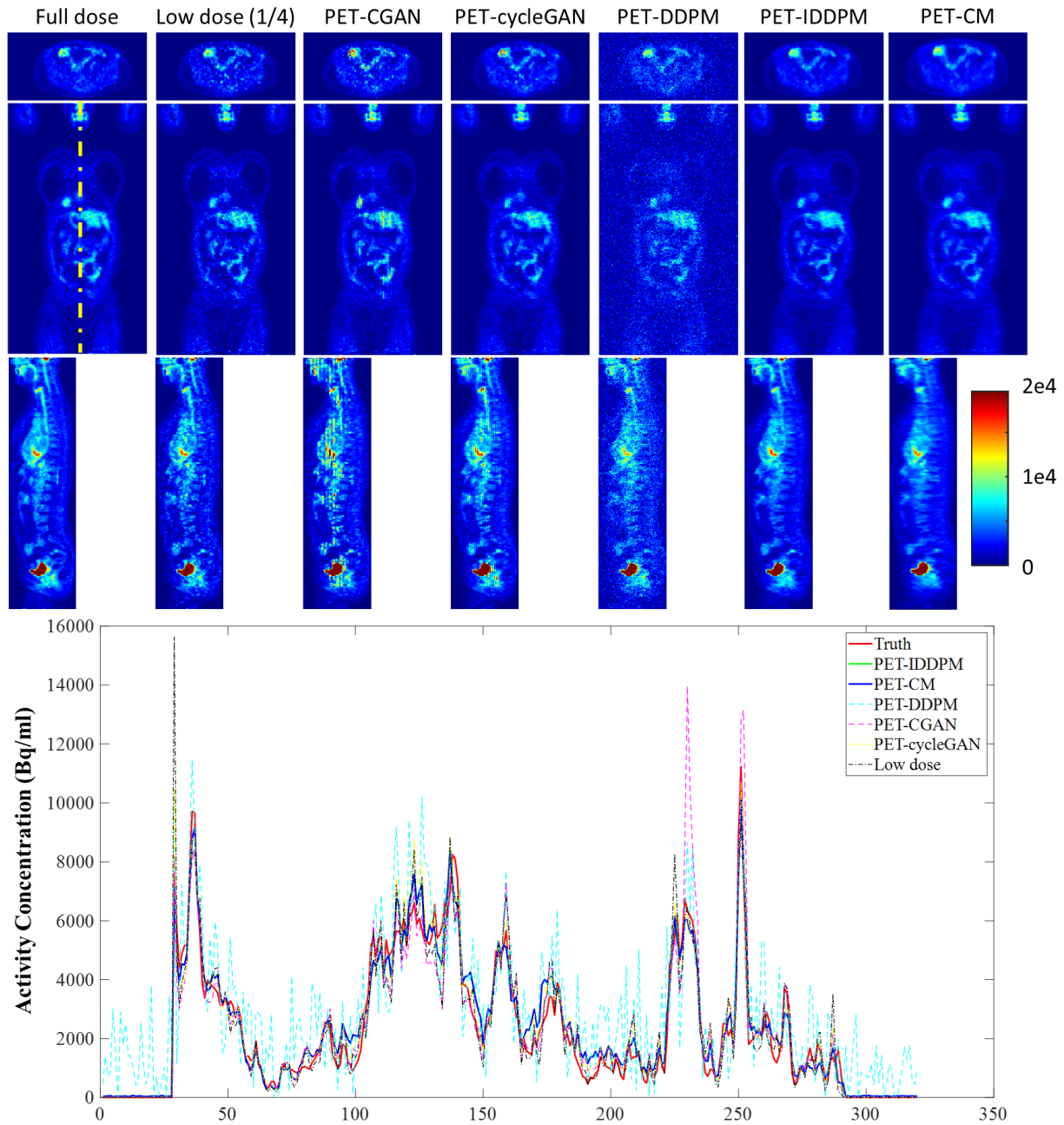


Figure 4: Visualization of the imaging results and single line profiles for the synthetic images obtained from 1/4 dose PETs. The figure displays the full dose image (1st column), the corresponding low dose image (2nd column), and the synthesized images generated by different methods: PET-DDPM (3rd column), PET-CGAN (4th column), PET-cycleGAN (5th column), PET-IDDPM (6th column), and PET-CM (7th column). The single line profiles are shown below the visualizations, illustrating the variations in intensity along the line for both the real and synthetic images. Red represents ground truth full-dose PET.

V. Result

Synthetic full-dose PETs generated from low-dose images using PET-CM and competing networks are presented in Figures 3 and 4, accompanied by single-line image profiles. To evaluate the quality of the synthetic images, we conducted quantitative assessments, the results of which are presented in Table. 1 for the eighth-dose PETs and Table. 2 for the quarter-dose PETs.

Table 1: Quantitative analysis of synthetic full-dose images from PET-CM vs. PET-CGAN, PET-cycleGAN, PET-DDPM, and PET-IDDPM using the eighth-dose PETs. (↑) indicates positive-orientation: greater values indicate better performance; (↓) indicates negative orientation: smaller values indicate better performance. The generation time (G-time) for each patient is reported. The best-performing network(s) are highlighted in bold, and the second-best network(s) are underlined, based on mean evaluation results. P-values between the competing networks and PET-CM are shown below each method. Values are rounded to three decimals.

1/8 dose to full dose	NMAE (%) (↓)	PSNR (dB) (↑)	SSIM (↑)	NCC (↑)	G-time (Sec)
PET-CM	<u>1.233±0.131</u>	33.915±0.933	<u>0.964±0.009</u>	0.968±0.011	62.321
<i>p-value</i>	N/A	N/A	N/A	N/A	
PET-IDDPM	1.224±0.13	<u>33.849±0.877</u>	0.966±0.009	0.968±0.012	823.713
<i>p-value</i>	0.552	0.665	0.726	0.748	
PET-DDPM	3.529±0.096	26.783±0.256	0.875±0.022	0.879±0.037	817.326
<i>p-value</i>	<0.010	<0.010	<0.010	<0.010	
PET-CGAN	2.329±0.482	27.349±1.758	0.948±0.013	0.946±0.015	32.142
<i>p-value</i>	<0.010	<0.010	<0.010	<0.010	
PET-cycleGAN	2.366±0.494	26.487±1.615	0.939±0.017	0.934±0.021	32.142
<i>p-value</i>	<0.010	<0.010	<0.010	<0.010	

Table 2: Quantitative analysis of synthetic full-dose images from PET-CM vs. PET-CGAN, PET-cycleGAN, PET-DDPM, and PET-IDDPM using the quarter-dose PETs. (↑) indicates positive-orientation: greater values indicate better performance; (↓) indicates negative orientation: smaller values indicate better performance. The generation time (G-time) for each patient is reported. The best-performing network(s) are highlighted in bold, and the second-best network(s) are underlined, based on mean evaluation results. P-values between the competing networks and PET-CM are shown below each method. Values are rounded to three decimals.

1/4 dose to full dose	NMAE (%) (↓)	PSNR (dB) (↑)	SSIM (↑)	NCC (↑)	G-time (Sec)
PET-CM	1.058±0.092	35.548±0.805	0.978±0.005	0.981±0.007	62.321
<i>p-value</i>	N/A	N/A	N/A	N/A	
PET-IDDPM	<u>1.083±0.085</u>	<u>35.404±0.684</u>	<u>0.977±0.006</u>	<u>0.980±0.008</u>	823.713
<i>p-value</i>	0.992	0.971	0.911	0.869	
PET-DDPM	3.361±0.057	27.264±0.14	0.887±0.022	0.898±0.035	817.326
<i>p-value</i>	<0.010	<0.010	<0.010	<0.010	

PET-CGAN	1.670±0.201	29.093±1.116	0.958±0.009	0.942±0.015	32.142
<i>p-value</i>	<0.010	<0.010	<0.010	<0.010	
PET-cycleGAN	1.470±0.14	30.931±0.775	0.963±0.009	0.955±0.017	32.142
<i>p-value</i>	<0.010	<0.010	<0.010	<0.010	

V.1 Comparison of eighth-dose to full-dose PETs

The PET-CM achieves the second-best results, with an NMAE of $1.233\pm 0.131\%$ and SSIM of 0.964 ± 0.009 , closely matching the best NCC of 0.968 ± 0.011 and PSNR of $33.915\pm 0.933\text{dB}$ achieved by the PET-IDDPM. Statistical analysis confirms that there is no significant difference between the PET-CM and PET-IDDPM. The PET-CM demonstrates significantly faster generation time than the PET-IDDPM (62 seconds vs. 823 seconds to generate one patient's image), though both proposed methods are slower than GAN-based methods. Comparatively, the proposed PET-CM exhibits substantial quantitative improvements at all metrics with statistical significance ($p < 0.05$) compared to other methods.

It is worth noting that PET-DDPM underperforms the GAN-based network on a large scale. This may be attributed to the fact that PET-DDPM can achieve comparable image synthesis to PET-IDDPM and PET-CM when the timestep is large (e.g., 1000 timesteps) (Pan *et al.*, 2023c; Peng *et al.*, 2023), but may not perform as well in our setting with only 50 timesteps. This limitation is visually evident in the generated images (Figures 2 and 3), where the presence of noise indicates that PET-DDPM is less effective in denoising. This further suggests that a limited number of timesteps hinders DDPM's ability to generate high-quality images through the effective elimination of noise.

V.2 Quantitative result of quarter-dose to full-dose PETs

The PET-CM also demonstrated the best performance with an NMAE of $1.058\pm 0.092\%$, PSNR of $35.548\pm 0.805\text{dB}$, SSIM of 0.978 ± 0.005 , and NCC of 0.981 ± 0.007 . Compared to the PET-IDDPM, the PET-CM does not show any statistical difference. However, when compared to other methods, the PET-CM shows significant quantitative and statistical improvements (all $p < 0.05$). This finding highlights the superiority of diffusion-based models over the commonly used GAN-based models in accurately estimating full-dose images from low-dose inputs.

VI. Discussion

In this study, we present an efficient diffusion-based PET consistency mode (PET-CM) model, which enables the generation of high-quality full-dose PETs from low-dose PETs. While state-of-the-art diffusion models, such as PET-IDDPM, are tailored to generate high-quality synthetic full-dose PET images, PET-

CM offers an efficient alternative for generating slightly lower quality images with significantly faster generation speeds. Our proposed low-dose to full-dose PET translation method has the potential to improve patient care by reducing both scan time and radiation exposure. This reduction in radiation dose, scan time and associated motion artifact may allow patients to obtain safer, high-quality images with accurate contrast and quantification. Although generative adversarial networks (GANs) are widely used for full-dose PET generation and demonstrate both impressive accuracy and realistic visual appearance, their utility is hindered by the presence of noise in both low-dose and full-dose PET data. This noise makes it challenging for GANs to effectively learn appropriate mappings, resulting in instability during training. Tuning the GAN hyperparameters to balance their generators and discriminators, stabilize the networks and generate reasonable full-dose sPETs requires considerable time. Furthermore, GANs are prone to instability during training which can lead to overfitting and mode collapse, limiting the quality of generated sPETs. In contrast, our methods overcome these limitations by eliminating adversarial training and the associated risk of mode collapse. These methods achieve state-of-the-art sPET quality without sacrificing network stability, eliminating the need for intensive hyperparameter tuning.

The proposed PET-CM involves two processes: a forward process and a reverse process. In the forward process, Gaussian noise is added to a clean full-dose PET image at each timestep, resulting in a sequence of noisy images. This process continues until the image becomes pure Gaussian noise. In the reverse process, a neural network (a Swin-ViT network) is employed to iteratively denoise the noisy images and restore them to the original state based on a corresponding low-dose PET image. The reverse process can be viewed as a translation from low-dose to high-dose PETs. The PET-CM model represents the reverse process: a consistency function which takes a noisy PET image and its corresponding timestep as input, with the expectation that the output of the function at each timestep should be identical to a clean image. Thus, the consistency function can estimate the clean full-dose PET image from a Gaussian noise sequence within a few steps (e.g., estimating the noisy image from T to $\frac{T}{2}$, and then to 0). To the best of our knowledge, this is the first diffusion-based consistency model for low-dose to full-dose PET image estimation.

As shown in Table 1, when estimating the full-dose PETs from the eighth-dose images, PET-CM methods exhibited remarkable quantitative improvements compared to most competing methods (PET-DDPM, PET-CGAN, and PET-cycleGAN). The PET-CM method demonstrated results comparable to PET-IDDPM with NMAE of $1.233\pm 0.131\%$, PSNR of $33.915\pm 0.933\text{dB}$, SSIM of 0.964 ± 0.009 , and NCC of 0.968 ± 0.011 , while requiring only 8% of PET-IDDPM’s generation time for each patient. In Table 2, the PET-CM methods demonstrated significant improvements compared to the PET-DDPM, PET-CGAN, and PET-cycleGAN. Specifically, PET-CM exhibited the best performance with NMAE $1.058\pm 0.092\%$, PSNR of $35.548\pm 0.805\text{dB}$, SSIM of 0.978 ± 0.005 , and NCC 0.981 ± 0.007 . Even though the proposed method requires

greater generation time than the competing GAN-based methods, these results highlight the effectiveness of PET-CM in estimating full-dose PETs from reduced dose inputs.

Although PET-CM exhibits impressive quantitative performance compared to GAN-based methods, it is important to note that these improvements are specifically observed in the context of 2D PET synthesis. In our empirical experiments, we have not been able to achieve reasonable performance using the PET-CM models in 3D PET synthesis. This diminished performance in 3D synthesis may be attributed to the limited complexity of the networks we explored. Our current hardware resources are insufficient to support the implementation of sufficiently large 3D networks for these methods. This limitation hinders our ability to accurately translate low-dose to full-dose 3D PETs, where obtaining spatial information across axial slices could potentially yield greater translation accuracy. Regardless, it is essential to recognize that these limitations do not undermine the value of PET-CM models. Instead, they underscore the need for further advancements to extend these models to 3D full-dose PET image estimation. Dorjsembe *et al.* (Dorjsembe *et al.*, 2022) propose a DDPM-based model for small size 3D magnetic resonance imaging (MRI) image synthesis, and Pan *et al.* (Pan *et al.*, 2023a) introduce a patch-based 3D Swin-UNET model based on IDDPM for MRI-to-CT image translations, demonstrating state-of-the-art performance. Memory-efficient techniques such as a self-supervised segmentation network (Lou *et al.*, 2022; Li *et al.*, 2023b), or distilling information from a large pre-trained foundation model (Hu *et al.*, 2023b; Li *et al.*, 2023a; Luan *et al.*, 2021) like ChatGPT (Liu *et al.*, 2023) or Segment-Anything (Kirillov *et al.*, 2023; Hu *et al.*, 2023a) into a smaller network could potentially enable image translation with limited hardware and achieve even better denoising and therefore better synthetic image quality. These examples suggest a future role for our proposed PET-CM models in 3D PET synthesis, enhancing the accuracy of the estimation process.

In future work, we plan to extend our models to support 3D low-dose to full-dose PET estimations. We intend to apply these methods to other modalities, such as MRI and ultrasound, providing a solution in medical applications where image samples are scarce, but high-quality images or volumes are needed.

VII. Conclusion

In this work, we have introduced a novel diffusion-based method for denoising and synthesizing full-dose PETs from low-dose PETs: the PET consistency model (PET-CM). The method successfully restores noisy PET images requiring one eighth to one quarter of the full dose required for standard high-quality PET images. This state-of-the-art diffusion-based model demonstrates state-of-the-art quantitative accuracy. PET-CM offers a negligible tradeoff in image quality for a thirteen-fold improvement in computational efficiency. PET-CM may prove a valuable tool for improving PET imaging by enabling radiation dose reduction without compromising diagnostic accuracy.

Acknowledgement

This research is supported in part by the National Institutes of Health under Award Number R56EB033332, R01EB032680, R01CA272991 and P30CA008748.

Conflict of interest

The authors have no conflict of interests to disclose.

Reference

- An L, Zhang P, Adeli E, Wang Y, Ma G, Shi F and Lin W 2016 Multi-Level Canonical Correlation Analysis for Standard-Dose PET Image Estimation *IEEE Transactions on Image Processing* **25** 1-
- Brix G, Lechel U, Glatting G, Ziegler S I, Münzing W, Müller S P and Beyer T 2005 Radiation Exposure of Patients Undergoing Whole-Body Dual-Modality ¹⁸F-FDG PET/CT Examinations *Journal of Nuclear Medicine* **46** 608-13
- Catana C 2019 The Dawn of a New Era in Low-Dose PET Imaging *Radiology* **290** 657-8
- Chaudhari A S, Mitra E, Davidzon G A, Gulaka P, Gandhi H, Brown A, Zhang T, Srinivas S, Gong E, Zaharchuk G and Jadvar H 2021 Low-count whole-body PET with deep learning in a multicenter and externally validated study *npj Digital Medicine* **4** 127
- Cherry S, Jones T, Karp J, Qi J, Moses W and Badawi R 2017 Total-Body PET: Maximizing Sensitivity to Create New Opportunities for Clinical Research and Patient Care *Journal of Nuclear Medicine* **59** jnumed.116.184028
- Dhariwal P and Nichol A 2021 Diffusion models beat gans on image synthesis *Advances in Neural Information Processing Systems* **34** 8780-94
- Dong X, Lei Y, Wang T, Higgins K, Liu T, Curran W J, Mao H, Nye J A and Yang X 2020 Deep learning-based attenuation correction in the absence of structural information for whole-body positron emission tomography imaging *Physics in Medicine & Biology* **65** 055011
- Dorjsembe Z, Odonchimed S and Xiao F *Medical Imaging with Deep Learning, 2022*, vol. Series)
- Gong K, Johnson K A, Fakhri G E, Li Q and Pan T 2022 PET image denoising based on denoising diffusion probabilistic models *arXiv preprint arXiv:2209.06167*
- He K, Zhang X, Ren S and Sun J *Proceedings of the IEEE conference on computer vision and pattern recognition, 2016*, vol. Series) pp 770-8
- Ho J, Jain A and Abbeel P 2020 Denoising diffusion probabilistic models *Advances in Neural Information Processing Systems* **33** 6840-51
- Hu M, Li Y and Yang X 2023a Skinsam: Empowering skin cancer segmentation with segment anything model *arXiv preprint arXiv:2304.13973*
- Hu M, Pan S, Li Y and Yang X 2023b Advancing Medical Imaging with Language Models: A Journey from N-grams to ChatGPT *arXiv preprint arXiv:2304.04920*
- Huda W, Sandison G A, Palser R F and Savoie D 1989 Radiation doses and detriment from chest X-ray examinations *Physics in Medicine & Biology* **34** 1477
- Kaplan S and Zhu Y 2018 Full-Dose PET Image Estimation from Low-Dose PET Image Using Deep Learning: a Pilot Study *Journal of Digital Imaging* 1-6
- Kirillov A, Mintun E, Ravi N, Mao H, Rolland C, Gustafson L, Xiao T, Whitehead S, Berg A C and Lo W-Y 2023 Segment anything *arXiv preprint arXiv:2304.02643*
- Lei Y, Dong X, Wang T, Higgins K, Liu T, Curran W J, Mao H, Nye J A and Yang X 2019 Whole-body PET estimation from low count statistics using cycle-consistent generative adversarial networks *Physics in Medicine and Biology* **64** 215017
- Li Y, Hu M and Yang X 2023a Polyp-sam: Transfer sam for polyp segmentation *arXiv preprint*

-
- arXiv:2305.00293*
- Li Y, Wynne J, Wang J, Qiu R L, Roper J, Pan S, Jani A B, Liu T, Patel P R and Mao H 2023b Cross-Shaped Windows Transformer with Self-supervised Pretraining for Clinically Significant Prostate Cancer Detection in Bi-parametric MRI *arXiv preprint arXiv:2305.00385*
- Liu Y, Han T, Ma S, Zhang J, Yang Y, Tian J, He H, Li A, He M and Liu Z 2023 Summary of chatgpt/gpt-4 research and perspective towards the future of large language models *arXiv preprint arXiv:2304.01852*
- Liu Z, Lin Y, Cao Y, Hu H, Wei Y, Zhang Z, Lin S and Guo B *Proceedings of the IEEE/CVF International Conference on Computer Vision, 2021*, vol. Series) pp 10012-22
- Lou A, Yao X, Liu Z and Noble J 2022 Min-Max Similarity: A Contrastive Learning Based Semi-Supervised Learning Network for Surgical Tools Segmentation *arXiv preprint arXiv:2203.15177*
- Luan T, Wang Y, Zhang J, Wang Z, Zhou Z and Qiao Y 2021 PC-HMR: Pose Calibration for 3D Human Mesh Recovery from 2D Images/Videos *Proceedings of the AAAI Conference on Artificial Intelligence* **35** 2269-76
- Lyu Q and Wang G 2022 Conversion Between CT and MRI Images Using Diffusion and Score-Matching Models *arXiv preprint arXiv:2209.12104*
- Nichol A Q and Dhariwal P 2021 Improved Denoising Diffusion Probabilistic Models. In: *Proceedings of the 38th International Conference on Machine Learning*, ed M Marina and Z Tong (Proceedings of Machine Learning Research: PMLR) pp 8162--71
- Pan S, Abouei E, Wynne J, Wang T, Qiu R L, Li Y, Chang C-W, Peng J, Roper J and Patel P 2023a Synthetic CT Generation from MRI using 3D Transformer-based Denoising Diffusion Model *arXiv preprint arXiv:2305.19467*
- Pan S, Chang C-W, Peng J, Zhang J, Qiu R L, Wang T, Roper J, Liu T, Mao H and Yang X 2023b Cycle-guided Denoising Diffusion Probability Model for 3D Cross-modality MRI Synthesis *arXiv preprint arXiv:2305.00042*
- Pan S, Wang T, Qiu R L, Axente M, Chang C-W, Peng J, Patel A B, Shelton J, Patel S A and Roper J 2023c 2D medical image synthesis using transformer-based denoising diffusion probabilistic model *Physics in Medicine and Biology*
- Peng J, Qiu R L, Wynne J F, Chang C-W, Pan S, Wang T, Roper J, Liu T, Patel P R and Yu D S 2023 CBCT-Based Synthetic CT Image Generation Using Conditional Denoising Diffusion Probabilistic Model *arXiv preprint arXiv:2303.02649*
- Saharia C, Ho J, Chan W, Salimans T, Fleet D J and Norouzi M 2022 Image super-resolution via iterative refinement *IEEE Transactions on Pattern Analysis and Machine Intelligence*
- Slomka P 2022 Future of nuclear cardiology is bright: Promise of cardiac PET/CT and artificial intelligence *Journal of Nuclear Cardiology* **29** 389-91
- Song J, Meng C and Ermon S 2020 Denoising diffusion implicit models *arXiv preprint arXiv:2010.02502*
- Song Y, Dhariwal P, Chen M and Sutskever I 2023 Consistency models *arXiv preprint arXiv:2303.01469*
- Unterrainer M, Eze C, Ilhan H, Marschner S, Roengvoraphoj O, Schmidt-Hegemann N S, Walter F, Kunz W G, Rosenschöld P M a, Jeraj R, Albert N L, Grosu A L, Niyazi M, Bartenstein P and Belka C 2020 Recent advances of PET imaging in clinical radiation oncology *Radiation Oncology* **15** 88
- Verger A, Kas A, Darcourt J and Guedj E 2022 PET Imaging in Neuro-Oncology: An Update and Overview of a Rapidly Growing Area *Cancers*
- Wang T, Lei Y, Fu Y, Curran W J, Liu T, Nye J A and Yang X 2020 Machine learning in quantitative PET: A review of attenuation correction and low-count image reconstruction methods *Physica Medica* **76** 294-306
- Wang Y, Yu B, Wang L, Zu C, Lalush D S, Lin W, Wu X, Zhou J, Shen D and Zhou L 2018 3D conditional generative adversarial networks for high-quality PET image estimation at low dose *NeuroImage* **174** 550-62
- Wang Y, Zhang P, An L, Ma G, Kang J, Shi F, Wu X, Zhou J, Lin W and Shen D 2016 Predicting Standard-Dose PET Image from Low-Dose PET and Multimodal MR Images Using Mapping-Based Sparse Representation *Physics in medicine and biology* **61** 791-812

-
- Xiang L, Qiao Y, Nie D, An L, Lin W, Wang Q and Shen D 2017 Deep auto-context convolutional neural networks for standard-dose PET image estimation from low-dose PET/MRI *Neurocomputing* **267** 406-16
- Zhang J, Chao H, Xu X, Niu C, Wang G and Yan P *Medical Image Computing and Computer Assisted Intervention–MICCAI 2021: 24th International Conference, Strasbourg, France, September 27–October 1, 2021, Proceedings, Part VI 24,2021*, vol. Series): Springer) pp 441-50